limnological review

Article

Assessing the Impact of Environmental Conditions on Reflectance Values in Inland Waters Using Multispectral UAS Imagery

Daniel Henrique Carneiro Salim [1], Gabriela Rabelo Andrade [1], Alexandre Flávio Assunção [1], Pedro Henrique de Menezes Cosme [1], Gabriel Pereira [1,2] and Camila C. Amorim [1,*]

[1] SIMOA—Intelligent Systems for Environmental Monitoring, Department of Sanitary and Environmental Engineering, Universidade Federal de Minas Gerais, Belo Horizonte 31270-901, MG, Brazil; danielhcsalim@gmail.com (D.H.C.S.); gabrielarabelo@gmail.com (G.R.A.); assuncfa@gmail.com (A.F.A.); pcosme555@gmail.com (P.H.d.M.C.); pereira@ufsj.edu.br (G.P.)

[2] Department of Geosciences, Universidade Federal de Sao Joao del-Rei, Sao Joao del-Rei 36301-158, MG, Brazil

* Correspondence: camila@desa.ufmg.br

Abstract: This study investigates the impact of environmental conditions on reflectance values obtained from multispectral Unmanned Aerial System (UAS) imagery in inland waters, focusing on sun glint, cloud glint, wind-generated waves, and cloud shading projections. Conducted in two reservoirs with differing water qualities, UAS platforms equipped with MicaSense Altum and DJI Phantom 4 Multispectral sensors were used to collect multispectral images. The results show that sun glint significantly increases reflectance variability as solar elevation rises, particularly beyond 54°, compromising data quality. Optimal flight operations should occur within a solar elevation angle range of 25° to 47° to minimize these effects. Cloud shading introduces complex variability, reducing median reflectance. Wind-generated waves enhance sun glint, increasing variability across all spectral bands, while cloud glints amplify reflectance non-uniformly, leading to inconsistent data variability. These findings underscore the need for precise correction techniques and strategic UAS deployment to mitigate environmental interferences. This study offers valuable insights for improving UAS-based monitoring and guiding future research in diverse aquatic environments.

Keywords: remote sensing; UAV; inland water; data analysis; sun glint

Citation: Salim, D.H.C.; Andrade, G.R.; Assunção, A.F.; Cosme, P.H.d.M.; Pereira, G.; Amorim, C.C. Assessing the Impact of Environmental Conditions on Reflectance Values in Inland Waters Using Multispectral UAS Imagery. *Limnol. Rev.* **2024**, *24*, 466–490. https://doi.org/10.3390/limnolrev24040027

Academic Editor: Andrzej Hutorowicz

Received: 28 June 2024
Revised: 25 August 2024
Accepted: 15 October 2024
Published: 29 October 2024

1. Introduction

Freshwater is one of the most vital human survival and well-being resources, as it sustains various aspects of life, including drinking water, agriculture, health, and industry. However, due to the increasing pressure of human activities, inland reservoirs are becoming more exposed to various forms of pollution from urbanization and industrialization. Therefore, it is crucial to effectively assess and monitor pollution in inland water if society wants to benefit from this valuable resource.

In situ field sampling provides detailed information at specific locations and times, but it is costly, time-consuming, and often needs to be repeated frequently. In contrast, remote sensing (RS) offers a synoptic, more comprehensive view across larger areas and over multiple periods [1,2]. As a complementary monitoring technique, RS can observe water quality from a local to a global scale with a revisit time of 3 days of public harmonized data [3], improve the efficiency of field operations by pinpointing pollution and anomaly hotspots [4], and produce water quality parameters modeling and mapping, such as chlorophyll-a concentration [5], turbidity [6], colored dissolved organic matter [7], phycocyanin [8], cyanotoxins [9], water clarity [10], among others.

Although satellite-based remote sensing techniques for measuring water reflectance generally offer suitable temporal and spatial resolution, they encounter significant limitations in detecting and monitoring rapid processes and phenomena with restricted spatial

extents [11]. These limitations become particularly pronounced when monitoring small and medium-sized water bodies that demand high spatiotemporal resolution or during emergency responses where timely data acquisition is crucial. Additionally, satellite observations are often hindered by cloud cover [12,13]. In this way, unmanned aerial systems (UASs) equipped with multispectral or hyperspectral sensors offer the capacity for observing small-scale variations in water surface and complement RS satellite analysis that suffers from mixed pixels and shore adjacency effects.

The UAS is a comprehensive platform encompassing the aerial vehicle itself, sensors, telemetry systems, ground-based workstations, and software for operating and controlling aerial missions. In addition to not requiring atmospheric corrections [14] and the potential to monitor regions with narrow water bodies [15] and urgent events that require high-frequency monitoring, UASs also show advantages for developing water quality parameters observations because of their easy deployment on-demand and portability for carrying multiple specific sensors [11].

Surface reflectance is a crucial remote sensing metric that provides important insights into the ecological and biogeochemical conditions of water bodies. Accurate measurements are essential for understanding water quality, as they involve separating the radiance coming from the water itself from the radiance reflected off the surface, enabling more precise environmental monitoring and management [16]. Variations in reflectance can serve as indicators of changes in the concentration of water constituents, temperature [17], clarity (Secchi disk depth) [18], and algal blooms [19], among others. However, the use of UASs in aquatic surface imaging is still a challenge. Factors such as sun, sky and cloud glints, wind-generated waves, and cloud shading can significantly introduce noise and affect the accuracy of reflectance measurements [20–22], which could potentially lead to misleading reflectance-based post-processing steps, such as water constituents' retrievals, feature extractions, and data analysis.

For instance, Ref. [20] demonstrated that the effects of sun glints and waves significantly affect the reflectance of images, with a standard deviation of 9.3% compared to only 2.8% for unaffected ones. In the realm of regression models for retrieving water parameters, models derived from calm water spectra consistently outperformed models that included these factors, showing higher co-relation values. In addition, Ref. [23] proposed an algorithm that integrates a Foreground Attention-based Semantic Segmentation Network (FANet) to correct sun glints and restore the texture of coral reefs in UAS-acquired Red-Green-Blue (RGB) imagery. This approach significantly enhanced the accuracy of the segmentation process, improving the subsequent task of coral reef mapping. Ref. [24] also emphasized the challenges and strategies for avoiding sun glint. They developed an artificial neural network that automatically detects sun glints in RGB images captured by UASs in shallow waters. The model achieved 99% accuracy, with a precision of 79% and a recall of 54%, showcasing its potential for conducting UAS as remote sensing in clean and shallow water. Ref. [16] compared four methods for removing sun glints to obtain more accurate RS retrievals of water constituents. The most effective method identified was a pixel-based analysis of near-infrared wavelengths to account for the sun glint. After corrections, the multiple linear regressions applied to UAS images' reflectance with in-situ chlorophyll-a and total suspended solids values resulted in 37% and 9% relative errors, respectively.

UAS images are more accurate in capturing the fine details of water surface reflectance; however, they are also more susceptible to noise from surface disturbances. This heightened sensitivity can lead to significant variations in reflectance values between adjacent pixels, creating challenges for accurate data interpretation. As the UAV's altitude increases, these surface noise effects merge and become less pronounced, leading to a smoother reflectance profile. However, this merging only partially eliminates the problem, as residual noise can still affect the overall accuracy of the reflectance data. Therefore, despite the benefits of high-resolution imagery, there remains a critical need for effective correction methods to mitigate the impact of water surface noise, ensuring that the high spatial detail does not come at the cost of data reliability [25].

Despite the potential of UASs in aquatic surface imaging, the precision of reflectance measurements is subject to influence by different environmental factors, with sun glint being the most extensively studied in the literature. However, the understanding of these influences remains incomplete, hindering the effective utilization of UASs for RS water quality monitoring. Thus, this study aims to provide a comprehensive analysis of the variability in reflectance measurements obtained from multispectral UAS images, considering the influence of key environmental factors such as sun glints, cloud glints, wind-generated waves, and cloud shading. The objective is to elucidate their impact on the reflectance readings in UAS imaging systems, ultimately aiming to improve the reliability and interpretability of UAS RS water quality monitoring data.

2. Material and Methods

2.1. Study Areas

This study analyzed two reservoirs and three distinct areas (Figure 1): the Vargem das Flores Reservoir, and the upstream and downstream sections of the Pampulha Reservoir, which are separated by a sediment control barrier. These areas were selected due to their size, usage, and water quality differences. Sun glint effects were analyzed using aerial images from the Vargem das Flores Reservoir, collected on 17 November 2021, using the sensor MicaSense Altum. For cloud glint, wind-generated waves, and cloud shading effects, images from both sections of the Pampulha Reservoir, collected on 10 March 2022, using the sensor FC6360 from DJI Phantom 4 Multispectral, were analyzed. The effects were examined independently: sun glint images from Vargem das Flores were compared only among themselves, while images of cloud glint, wind-generated waves, and cloud shading were analyzed separately for the upstream and downstream sections of Pampulha. This approach minimized interference from water quality differences between the two Pampulha sections.

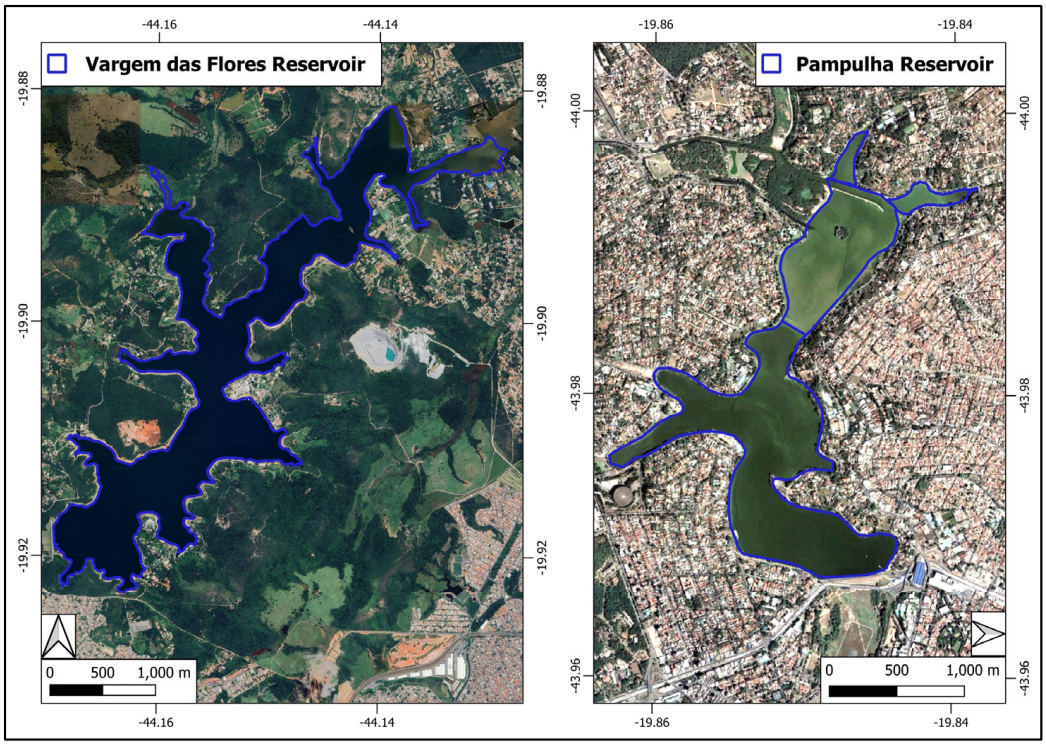

Figure 1. Localization of study area. Vargem das Flores (**left**) and Pampulha upstream and downstream to the net (**right**) reservoirs are located in the metropolitan area of Belo Horizonte City, Brazil.

2.1.1. Vargem das Flores Reservoir

The Vargem das Flores Reservoir (Figure 1 (left)) is situated in the metropolitan area of Belo Horizonte, Minas Gerais State (S 19.8959054 W 44.1482116). It is primarily used for urban water supply and is characterized by clear waters with low turbidity and chlorophyll levels. The reservoir covers an area of 5.5 km^2, has a maximum depth of 25 m, and holds a volume of approximately 40 hm^3. The reservoir is managed by the company Companhia de Saneamento de Minas Gerais.

2.1.2. Pampulha Reservoir

The Pampulha Reservoir (Figure 1 (right)), located in Belo Horizonte (S 19.8512955 W 43.9796154), has been recognized as a UNESCO Cultural Heritage site since 2016. This reservoir is a key example of Brazil's modernist architectural movement, initiated in 1940. Despite its cultural significance, the reservoir has suffered from eutrophic conditions since 1984 [26]. The reservoir is within a densely populated hydrological basin and receives significant inflows of untreated wastewater and rainwater runoff, containing high levels of sediments, organic matter, and nutrients. It covers an area of 2.6 km^2, has a maximum depth of 16 m, and holds a volume of approximately 10 hm^3. Currently, the reservoir is managed by the Municipality of Belo Horizonte. Notably, a sediment control barrier within the reservoir creates two distinct water characteristics: upstream of the barrier, the water has a brown hue, while downstream, it exhibits a predominantly green tint.

2.2. Unmanned Aircraft Systems

Two commercial UASs, designed for photogrammetric multispectral mapping and equipped with downwelling sunlight sensors to measure irradiance at the time of image capture, were employed to capture multispectral images of the reservoirs:

(i) NUVEM-ALTUM UAS: A semi-integrated UAS equipped with a MicaSense Altum sensor mounted on a Nuvem Spectral UAV. This UAS was controlled via a radio controller, with mission planning conducted using NCONTROL software on a laptop. A USB telemetry antenna was connected to the laptop to enable telemetry. The gimbal system has a single-axis configuration fixed at a -90° nadir angle, with the sensor azimuth angle aligned with the flight direction.

The spectral configuration for the MicaSense Altum sensor is as follows: Blue at 475 ± 20 nm, Green at 560 ± 20 nm, Red at 668 ± 10 nm, Red-Edge at 717 ± 10 nm, Near-Infrared (Near-IR) at 840 ± 40 nm, and Thermal Infrared LWIR at 8–14 μm. The spatial resolution is 3.2 MP (2064×1544) for the multispectral channels and 160×120 pixels for the LWIR channel.

(ii) DJI P4M UAS: The DJI Phantom 4 Multispectral is equipped with an integrated FC6360 camera. This UAS was fully designed by the original manufacturer. It was controlled using an SDK remote controller, with mission planning conducted on a tablet running the DJI GS Pro app. A versatile 3-axis gimbal system allows for a wide range of motion, enabling tilt adjustments from -90° (nadir angle) to $+30^\circ$.

The spectral configuration for the DJI P4M UAS is as follows: Blue at 450 ± 16 nm, Green at 560 ± 16 nm, Red at 650 ± 16 nm, Red-Edge at 730 ± 16 nm, and Near-IR at 840 ± 26 nm, with a spatial resolution of 2.1 MP (1300×1600). Additionally, the DJI P4M UAS includes an RGB Panchromatic band and features a First-Person View (FPV) capability.

2.3. Collection of UAS Images

2.3.1. Sun Glint Effect

To study the impact of sun glint on the reflectance of inland water in UAS imagery, the UAS missions over the Vargem das Flores Reservoir were meticulously planned to capture this effect under varying sun-sensor geometries. Sun glint occurs when sunlight is directly reflected off the water surface towards the sensor, increasing the measured radiance that does not originate from the water column. The intensity of sun glint is highly dependent

on the solar-sensor geometry and the surface roughness of the water, which is influenced by wind speed and other environmental factors [16].

The imagery was collected using the NUVEM-ALTUM UAS during 15-min photogrammetric flights with 75% longitudinal overlap and 65% side overlap. These flights were conducted at an altitude of 100 m. To minimize unwanted scattering of sun glint along the flight paths, the mission planning ensured that the UAS sensor's azimuth angle—aligned with the flight direction due to the fixed gimbal—was intentionally matched with the average Solar Azimuth Angle for each mission time [27,28]. Figure 2 illustrates the flight paths for each mission. Only images capturing the water surface were analyzed, while those containing terrestrial features were excluded.

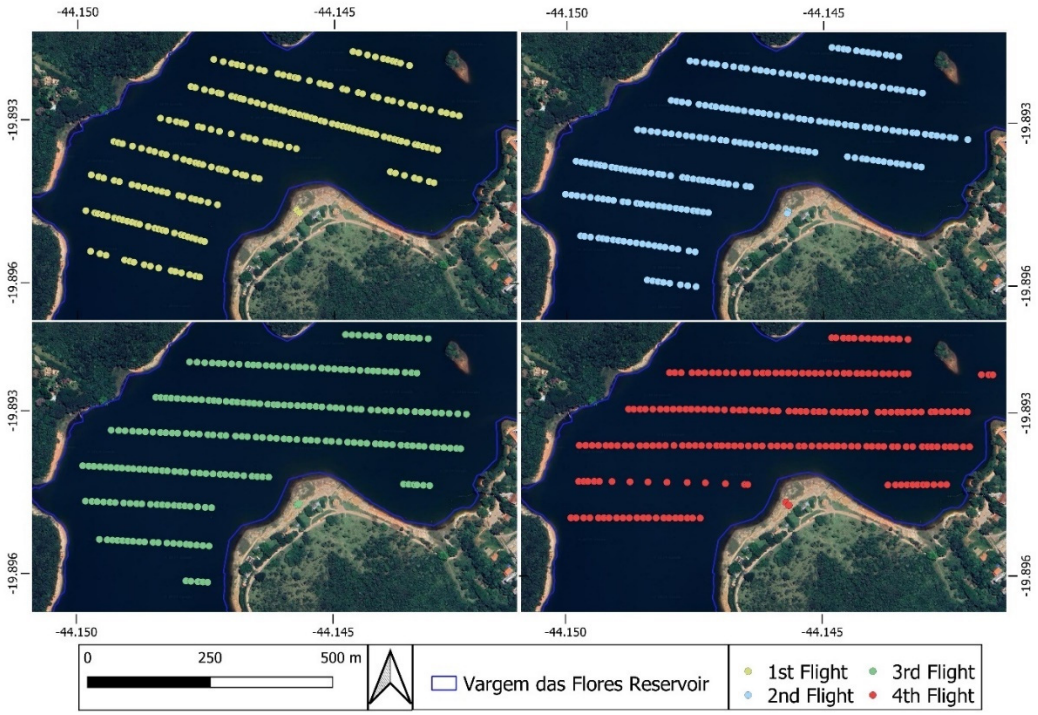

Figure 2. Flight paths of the UAS missions conducted over Vargem das Flores Reservoir to study the impact of sun glint on water reflectance. Each colored dot represents the coordinates of images for a mission: 1st Flight (yellow), 2nd Flight (light blue), 3rd Flight (green), and 4th Flight (red).

Literature was considered to analyze the sun glint effects caused by the Solar elevation angle. Ref. [27] advised maintaining a Solar elevation angle between 30° and 45°, while [29] suggested angles between 30° and 60°. Ref. [28] recommended using glint removal procedures for angles ranging from 35° to 75°. Additionally, Ref. [30] recommended a maximum Solar elevation angle of 90° minus half the field of view (FOV) of the camera sensor.

Given the available battery capacity, during springtime, flights were scheduled to start at the beginning of each hour from 07:00 to 10:00 AM on 17 November 2021 (see Table 1). This schedule allowed for the assessment of a wide range of solar elevation angles, ensuring comprehensive data collection for the analysis. Weather conditions were sunny (no clouds) with wind speeds below 1 m/s. In Table 1, the multiplication factor (*5) denotes the sensor's acquisition of imagery across five distinct spectral bands (Blue, Green, Red, RedEdge, and Near-Infrared). Each set of five images represents a single multispectral scene.

Table 1. UAS Flight and Solar Data for Sun Glint Analysis with NUVEM-ALTUM UAS at Vargem das Flores.

Flight Number	Multispectral Images	Time (GMT-3)	Solar Elevation	Solar Azimuth	Sensor Azimuth
1st	222 × 5 = 1110	07:02–07:19	24.9°–28.8°	102.4°–101.3°	103
2nd	219 × 5 = 1095	08:21–08:37	43.1°–46.9°	97.8°–96.9°	97
3rd	256 × 5 = 1280	09:09–09:24	54.3°–57.8°	95.2°–94.3°	93
4th	232 × 5 = 1160	10:08–10:22	68.2°–71.5°	91.7°–90.7°	90

Note: The multiplication factor (×5) indicates that each flight captured images across 5 spectral channels (Blue, Green, Red, RedEdge, Near-IR). Thus, each set of 5 images represents one complete multispectral scene.

2.3.2. Cloud Glints, Wind-Generated Waves, and Cloud Shading Projections Effects

Studying the effects of environmental conditions, such as cloud glints, wind-generated waves, and cloud shading projections, presents a challenge due to the unpredictability of these phenomena. This contrasts with the more prepared procedure for collecting sun glint data. These effects cannot be planned for specific flights as they depend on minor, sudden, and unpredictable changes in environmental conditions. Images exhibiting these effects were sourced from a research project aimed at modeling aquatic constituent concentrations (chlorophyll, turbidity, and phycocyanin) using UAS Remote Sensing.

Therefore, the images captured by the DJI P4M UAS at the Pampulha Reservoir on 10 March 2022, during summertime, were specifically selected because they displayed these phenomena. The day featured intermittent cloud cover, and ground wind speeds ranged from 1 to 3 m/s at the take-off area. To minimize strong sun glint effects caused by high solar angles, available images were selected between 07:34 and 10:06 AM when solar elevation was between 23° and 54°.

Given the varying water qualities in the Pampulha Reservoir, the UAS images were initially sorted based on their location, either upstream or downstream of the net barrier controlling sediment propagation. To further assess the spectral response concerning different water qualities, surface water quality measurements were taken using the YSI EXO2 Multiparameter Water Quality probe on the same day of UAS data collection. Measurements were conducted both upstream and downstream of the sediment retention net. The median values recorded upstream (N = 16) and downstream (N = 8) of the net were 13.9 and 9.1 relative fluorescence units (RFU) for chlorophyll-a and 54.6 and 7.1 Formazin Nephelometric Units (FNU) for turbidity, respectively.

The similar median chlorophyll-a values at both locations suggest comparable algae levels. However, the pronounced difference in turbidity indicates a significantly higher concentration of suspended sediments upstream. This difference can be attributed to the net, which slows down the water velocity, favoring sedimentation before the water crosses the net downstream. This mechanism likely reduces the amount of suspended fine-grained particles in the water downstream of the net, leading to lower turbidity readings downstream. This supports separating the reservoir into two distinct environments to independently analyze the effects of cloud reflections, wind-generated waves, and cloud shading projections.

Subsequently, the categories “upstream of the net” and “downstream of the net” were divided into affected and non-affected groups based on the visual perception of sky glints, waves, and shading projections, as illustrated in Figure 3. Non-affected images were those minimally or not influenced by these interferences. Within this framework, we independently compared the outcomes of each environmental condition. The details of the image dataset are presented in Table 2.

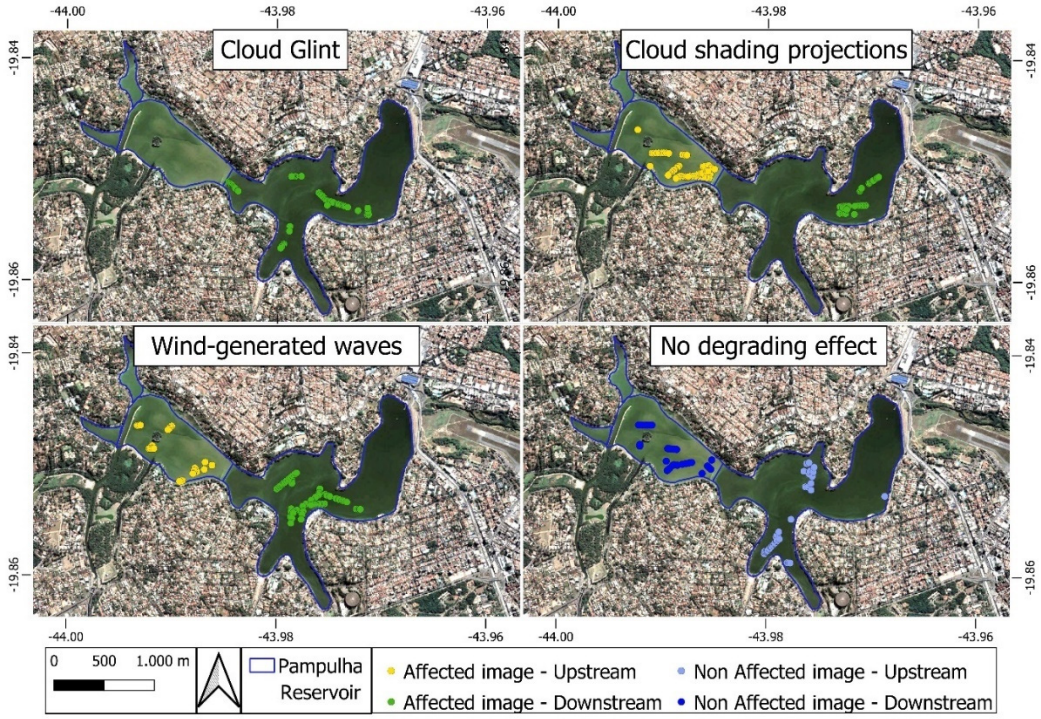

Figure 3. Spatial distribution of DJI P4M UAS images in the Pampulha Reservoir (10 March 2022) categorized by the effects of cloud glints, wind-generated waves, and cloud shading projections. The images are divided into upstream (west section) and downstream (east section) of the sediment retention net.

Table 2. Multispectral image dataset for comparing degrading effects upstream and downstream with DJI P4M UAS at the Pampulha Reservoir.

Degrading Effect	Multispectral Images (Upstream of the Net)	Time (GMT-3)	Multispectral Images (Downstream of the Net)	Time (GMT-3)
Cloud glint	-	-	47 × 5 = 235	07:34–09:28
Wind-generated waves	24 × 5 = 120	09:28–09:42	53 × 5 = 265	07:35–08:39
Cloud shading projections	52 × 5 = 260	09:14–09:48	32 × 5 = 160	08:35–10:06
No degrading effect	31 × 5 = 155	09:20–09:49	39 × 5 = 195	07:38–09:58

Regarding exposure settings during image collection, both UASs used the automatic exposure mode rather than manually configuring values for focal length, ISO, and exposure time. We adopted this approach because when sun glint affects the sensor or terrestrial land appears in the sensor's view, the ISO and exposure time automatically adjust to the new brightness conditions. Additionally, it is impractical to manually adjust exposure settings for each image collection, particularly without a first-person view, as is the case with the MicaSense Altum. Ref. [31] used auto mode in the MicaSense sensor but expressed concerns about the impact on image quality and subsequent processing. Moreover, after testing six different exposure settings, Ref. [32] confirmed the high efficiency and accuracy of the auto mode of the DJI P4M UAS.

2.4. Processing of Multispectral UAS Imagery

Due to the spectral properties of water, which result in lower reflectance signals compared to terrestrial targets, it is crucial to perform reflectance calibration to effectively distinguish clear water from turbid water and chlorophyll algae blooms [33,34].

In this study, the radiometric calibration process for multispectral UAS imagery involves capturing irradiance data from both a ground-based Calibration Reflectance Panel (CRP) and a Downwelling Light Sensor (DLS) mounted on the drone. The CRP reflects incoming radiation, and given its known reflectance properties, this reflected radiance can be used to calculate the incoming irradiance for each spectral band. Concurrently, the DLS sensor, positioned on top of the drone facing the sky, measures the downwelling irradiance directly. The CRP tracked changes in irradiance before and after each flight, while DLS captured irradiance levels precisely at the moment of each photo, which is crucial for detecting sudden changes like cloud cover.

The DLS sensors used were manufactured by DJI and MicaSense. However, the CRP from MicaSense was employed to calibrate images from both sensors, as DJI does not provide a CRP for their multispectral sensor. This decision was influenced by previous successful calibrations using non-specific reflectance panels by [32,35].

The selected samples were calibrated using Agisoft Metashape 2.0 software. To achieve precise radiometric calibration in Metashape, the methodology for both UAS images leverages the comprehensive model provided by MicaSense (GitHub: MicaSense RedEdge and Altum Image Processing Tutorials. 2024. Available online: https://github.com/micasense/imageprocessing (accessed on 19 August 2024).). At the first step of radiometric calibration, raw data obtained from the multispectral UAS sensor were converted into absolute spectral radiance (L_{UAS}) (W m^{-2} sr^{-1}). This model converts raw pixel values from the captured images into absolute spectral radiance values, accounting for various factors including sensor black level, sensitivity, gain, exposure settings, and lens vignette effects. All necessary parameters are extracted from the image metadata. The pixel values are normalized by dividing them by 2N (where N is the bit depth of the image), converting them into a range from 0 to 1. The vignette model corrects for light sensitivity fall-off in pixels further from the center by applying a polynomial function, whose parameters are also stored in the metadata. The correction process followed the equation:

$$L_{UAS}(\lambda) = V(x,y) \times \frac{a_1}{g} \times \frac{p(\lambda) - p_{BL}}{t_e + a_2 y - a_3 t_e y} \quad (1)$$

where: p is the raw pixel value, p_{BL} is the black level value, a_1, a_2, a_3 are the radiometric calibration coefficients, $V(x, y)$ is the vignette polynomial function for pixel location (x, y), t is the image exposure time, g is the sensor gain setting.

The systematic differences between the irradiance measurements obtained from the CRP and DLS can significantly impact the accuracy of the reflectance values derived from multispectral UAS imagery. Equations (2) and (3) address these differences by providing a correction factor, $Cor(\lambda)$, that adjusts the reflectance values recorded by the UAS sensor. This correction factor is derived from the linear relationship between the irradiance measured by the CRP ($IRR_{CRP}(\lambda)$) and the DLS ($IRR_{DLS}(\lambda)$), encapsulated in the coefficients a and b. These coefficients are determined through a regression analysis accounting for the sensors' spectral responses, sun-sensor geometry, and atmospheric scattering, among other environmental conditions [36].

$$Irr_{CRP}(\lambda) = a \times Irr_{DLS}(\lambda) + b \quad (2)$$

$$Cor(\lambda) = \frac{a}{1 - \frac{(b \times R_{CRP})}{\pi \times L_{CRP}(\lambda)}} \quad (3)$$

The MicaSense CRP used in this study is constructed from materials that exhibit diffuse reflectance, meaning they scatter incident light uniformly in all directions, a characteristic typical of Lambertian surfaces. These surfaces reflect light equally regardless of the observation angle, making them ideal for accurate calibration purposes.

Equation (4) further refines the reflectance calculation by normalizing the radiance values L_{UAS} with the irradiance measured by the DLS, and then applying the correction factor $Cor(\lambda)$. This normalization process is essential because the irradiance recorded by the DLS reflects the instantaneous light conditions during each image capture, accounting for transient changes such as cloud cover or varying solar angles. As a result, the corrected reflectance $R_{UAS\,COR}(\lambda)$ provides a more reliable representation of the true surface properties.

$$R_{UASCOR}(\lambda) = \frac{L_{UAS}(\lambda)}{Irr_{DLS}(\lambda)} \times Cor(\lambda) \quad (4)$$

Worth noting that when capturing the photo of the CRP, the DJI P4M UAS sensor was approximately 50 cm away from the panel, and the MicaSense Altum was around 100 cm away. In this manner, the images containing the QR code and the panel target were sharp (not blurred) and easily recognized during calibration steps.

The radiometrically calibrated images were then imported into a Python script and resized by a factor of 1/10 for both width and height, thereby reducing the number of pixels by a factor of 1/100. This step was necessary to ensure that the processing servers could handle and process the amount of data extracted from all the samples of each group.

2.5. Statistical Analysis of Reflectance Values

The statistical analysis of reflectance values aimed to elucidate the effects of environmental conditions, such as sun glint, cloud glint, wind-generated waves, and cloud shading projections, on UAS imagery. The calibrated reflectance values were categorized based on these conditions and further divided by spectral bands (Blue, Green, Red, Red Edge, and Near-IR). Summary statistics, including mean, standard deviation, Coefficient of Variation, and Signal-to-noise Ratio were calculated for the pixels in each categorized group and across different spectral bands to provide insights into the central tendency, variability, and data quality.

The mean provides the average reflectance value for each group, representing the central tendency of the data. The standard deviation (Std Dev) measures the spread or dispersion of reflectance values around the mean, indicating the level of variability in the data. A higher standard deviation suggests greater variability. The Coefficient of Variation (CoV) is a standardized measure of dispersion, calculated as the ratio of the standard deviation to the mean. It allows for comparisons of variability between different spectral bands and conditions, regardless of the magnitude of the reflectance values. A higher CoV indicates greater relative variability. The Signal-to-Noise Ratio (SNR) compares the magnitude of the signal (mean reflectance) to the level of noise (standard deviation). A higher SNR indicates that the signal is stronger relative to the noise, suggesting that the reflectance data are more reliable and less affected by environmental disturbances.

Boxplots and Probability density functions (PDFs) were plotted to visualize the distributions and identify notable patterns. Symbols in boxplots are lower and upper outliers represented by dots below and beyond the whisker, the minimum and maximum values at the bottom and top of the whisker, the first quartile and third quartile at the lower and upper edge of the box, and the median as an orange horizontal line within the box. The statistical analyses were performed using Python with libraries such as NumPy, SciPy, and Pandas for data manipulation and calculations. Visualization was carried out using Matplotlib to generate PDF plots and other graphical representations.

3. Results

3.1. Sun Glint

The study aimed to analyze the variations in sun glint effects at different times of the day during UAS (Unmanned Aerial System) flights. Data were collected using the NUVEM-ALTUM UAV, capturing five spectral bands: Blue, Green, Red, Red Edge, and Near-IR. The flights were conducted on a sunny day at four specific times: 07:02 AM, 08:21 AM, 09:09 AM, and 10:08 AM, on 17 November 2021, at the same spot on Vargem das Flores

Reservoir, with ground wind speeds below 1 m/s. Therefore, variations in reflectance are likely related to the sun-sensor geometry rather than water quality differences and the glint and shadows observed in waves and cloudy conditions.

Figure 4 presents a boxplot analysis of the reflectance values across these times and spectral bands. Additionally, Figure S1 provides a complementary visualization of the same data, with a Y-axis scale ranging from 0 to 0.15 for the first two flights and from 0 to 1.00 for the last two flights.

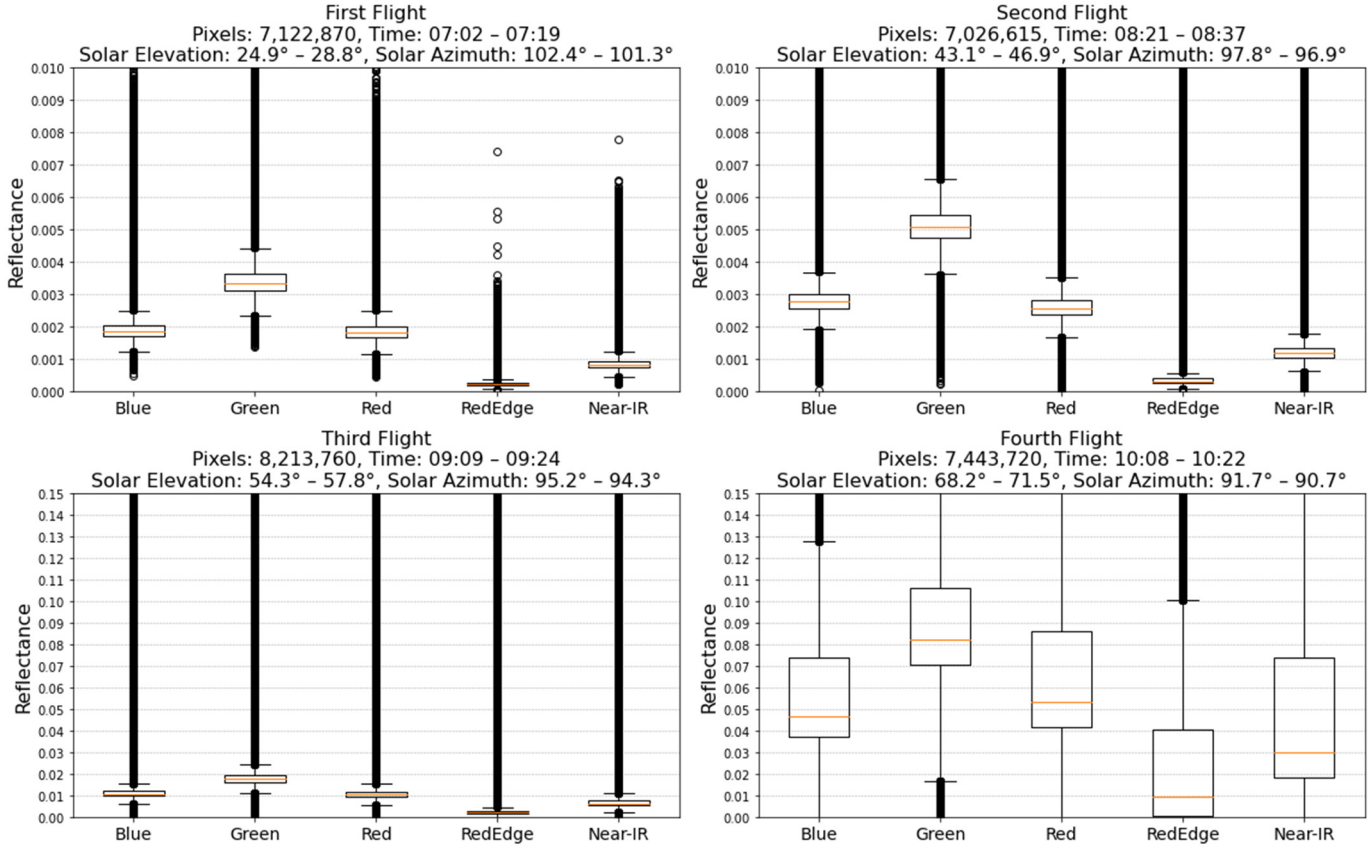

Figure 4. Boxplot analysis of pixels' reflectance values for five spectral bands (Blue, Green, Red, Red-Edge, Near-IR) across four NUVAM-MICASENSE UAS flight times (07:02 AM, 08:21 AM, 09:09 AM, and 10:08 AM) on 17 November 2021, at Vargem das Flores Reservoir. The orange line represents the median reflectance for each band, indicating the central tendency of the data distribution.

The spectral behavior remained consistent across all four flights, with the Green band showing higher mean reflectance than the Blue and Red bands, caused by the absorption characteristics of chlorophyll-a in low turbidity waters [37,38]. The Red Edge and Near-IR bands exhibited lower reflectance values compared to the visible bands, which can be explained by the high water absorption coefficient in the infrared [39]. Moreover, there was a slight increase in Near-IR reflectance, which could be associated with mineral and organic suspensions [40].

From the first to the fourth flight, the boxplots revealed a systematic increase in the minimum, median, maximum, and quartile values. Simultaneously, lower outliers decreased. In addition, the data distribution became more dispersed, with an increase in the interquartile range (IQR) and the number of outliers, indicating greater variability as the solar elevation angle increased. The low irradiance reaching the water surface likely prevented the occurrence of glint in the early flights. For instance, the Green band's median values increased from 0.0034, 0.0051, and 0.018 in the first three flights to 0.081 in the fourth flight, representing a relative increase of 50%, 252%, and 350% compared to the previous

flight. Similarly, the Green band's maximum values rose from 0.0045, 0.0066, and 0.0245 to 0.1671, reflecting a relative increase of 46%, 271%, and 583%.

Figure 5 provides a detailed statistical analysis, showing the mean, CoV, standard Std Dev, and SNR for each spectral band and flight time, along with the PDF of the reflectance values. This figure is crucial for understanding the impact of sun glint on the data's quality and distribution. The histograms within the figure are normalized so that the area under the curve sums to one, offering a probabilistic view of the reflectance values. Higher peaks in the density indicate more frequent reflectance values, while flatter areas signify less frequent values.

The data reveal a clear pattern where, as the sun's elevation angle increases, the CoV, Std Dev, and mean across all spectral bands also rise, following the trend: 4th flight > 3rd flight > 2nd flight > 1st flight. This simultaneous increase in CoV, Std Dev, and median reflects greater variability and a shift in central tendency in the reflectance values due to the intensifying sun glint, which escalates with the sun's elevation. Conversely, an inverse relationship is observed with the SNR, which decreases as the sun glint increases. For example, comparing the first and the fourth flights, the Red band means increased from 0.0018 to 0.1290, CoV rose from 0.15 to 1.63 and SNR decreased from 6.52 to 0.62.

This suggests that the data quality diminishes with increased sun glint, as noise becomes more pronounced relative to the signal. The decrease in SNR and the corresponding increase in CoV and Std Dev can be observed through the reduction in the density peak from the first to the fourth flight and the broadening of the base of the density curve.

Furthermore, as illustrated in the boxplot, the variability and central tendencies between the first and second flights are minimal, in contrast to the significant increase observed in the third and fourth flights, which indicates a corresponding decline in data quality. Therefore, to utilize the images from the third and fourth flights—where solar elevation angles exceed 54.3°—for developing products that require precise and consistent reflectance measurements, it is crucial to apply appropriate corrections to the imagery beforehand, as recommended by [28]. Given that higher noise levels necessitate greater caution in both the application and interpretation of results, the sun glint correction process must be meticulously detailed to address the complexities related to the magnitude and variability of the data

Our findings agree with those of [30], who recommended a maximum solar elevation of 58.7° for sensors with an FOV of 62.7°, as our study demonstrates that sun glint at this solar elevation (third flight) significantly compromised the magnitude and distribution of the reflectance readings in this case. Furthermore, our results partially agree with [27] who advocate for conducting flights when the solar elevation is between 30° and 45°. These conditions, approximately corresponding to our first (24.9° to 28.8°) and second (43.1° to 46.9°) flights, yielded the lowest CoV and the highest SNR. Therefore, provided that the sensor's azimuth is aligned with the solar azimuth, the optimal interval for capturing images without strong sun glint effects over aquatic reservoirs can be extended to a solar elevation range between 25° and 47°.

The results underscore the necessity of carefully selecting sensor azimuth and flight times to mitigate the impact of sun glint and to ensure the acquisition of high-quality data for applications involving reflectance-based products.

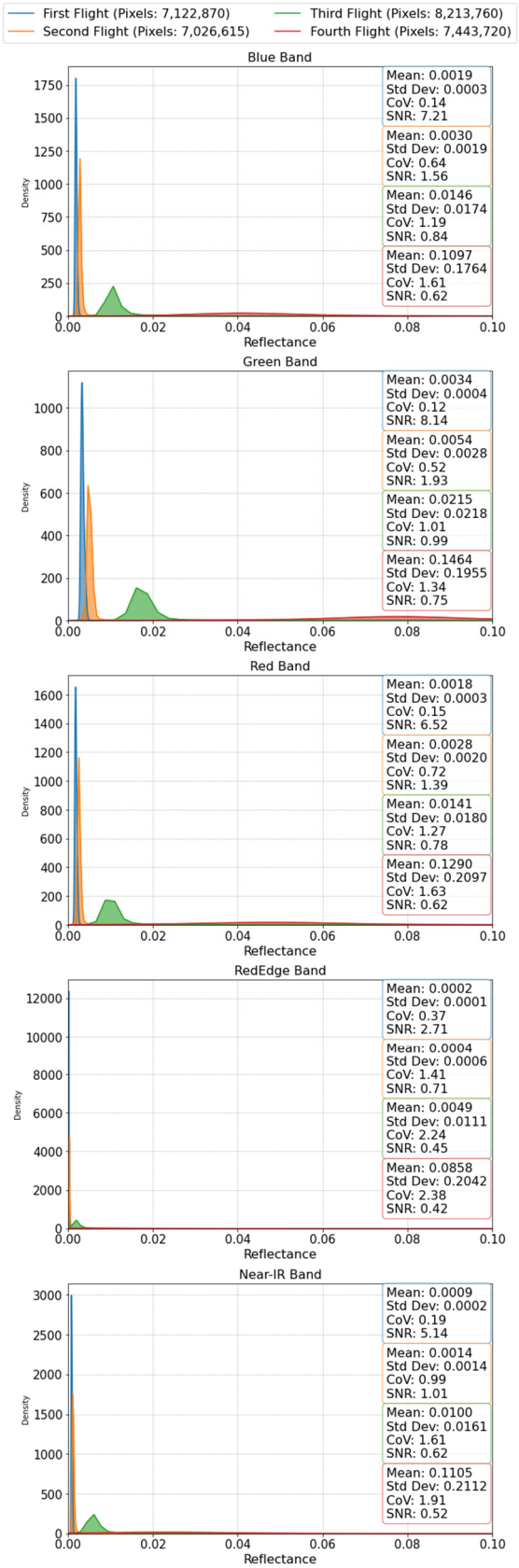

Figure 5. Probability density functions of reflectance and flight times referring to the impact of sun glint in NUVEM-ALTUM UAS-based remote sensing at Vargem das Flores Reservoir on 17 November 2021.

3.2. Cloud Shading, Wind-Generated Waves and Sky Glint

3.2.1. Pampulha Reservoir—Upstream of the Net

The analysis of spectral responses under varying environmental conditions—specifically cloud glints, wind-generated waves, and cloud shading—reveals distinct variations in the reflectance values of pixels from images captured at the Pampulha Reservoir. The images, taken during the DJI P4M UAS survey on 10 March 2022, were classified into affected and non-affected groups based on visual identification of these phenomena. These groups were further divided into upstream and downstream categories, allowing for an independent comparison of each environmental condition's impact on the spectral behavior of the water surface. Images categorized as upstream of the net were collected between 09:14 and 09:49; therefore, glints caused by solar elevation are not considered in this section. Figure 6 presents boxplots that illustrate these comparisons, highlighting the differences in reflectance values under these varied conditions.

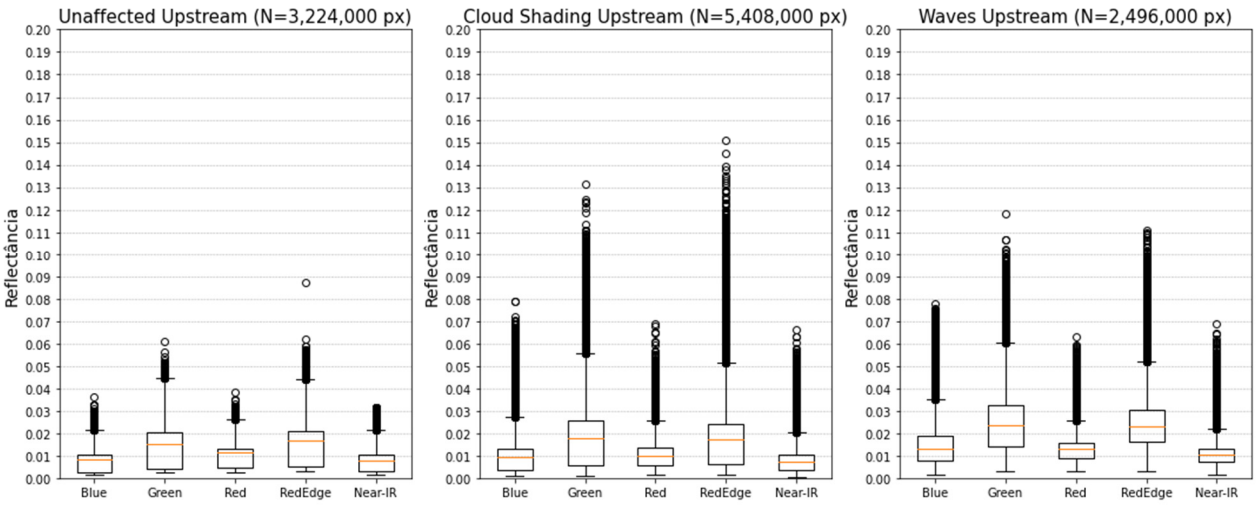

Figure 6. Boxplot analysis of pixel reflectance values under different environmental conditions at the Pampulha Reservoir (upstream of the net) on 10 March 2022, collected with DJI P4M UAS. The orange line represents the median reflectance for each band, indicating the central tendency of the data distribution.

For the cloud shading condition, although no clear trend was observed in the median reflectance values across the five multispectral bands, there was a notable decrease in minimum values, along with an increase in the third quartile (Q3), maximum values, and the length of the upper tail of outliers.

These distribution changes can be attributed to the camera's exposure adjustments in response to varying light conditions. When cloud shading reduces overall illumination in the scene, the sensor automatically increases its ISO sensitivity to capture details in low-light areas. However, this adjustment can inadvertently lead to over-saturation in non-shaded pixels, resulting in higher reflectance values for Q3, maximum, and outliers. The reduction in minimum values is linked to pixels that remain shaded despite the sensitivity adjustment.

This outcome aligns with the unpredictability and challenges noted [20], which demonstrated that the impact of shadow on UAS water reflectance is complex, with no consistent trend observed across different scenarios. The uncertainty in reflectance values may be caused by changes in the relative proportions of bright versus shaded areas in the images, as well as abrupt reflectance changes associated with incident angles and line-of-sight interactions due to the roughness of waves [41].

In the presence of waves, the boxplot analysis demonstrates a generalized increase in reflectance values, as evidenced by elevated first and third quartiles, maximum values, and upper outliers, as well as higher median values across all bands. This pattern suggests wave-induced variability in reflectance data is primarily due to enhanced sun glint, resulting from the dynamic reflection angles on the water surface. These observations are consistent with [21], which indicates that waves significantly increase sun glint, raising reflectance values and broadening their distribution compared to unaffected areas.

Figure 7 (left) presents the PDF of pixel reflectance values from each band, categorized by the presence or absence of the phenomena in images from upstream to the net area of the Pampulha Reservoir. A distinct differentiation is observed when analyzing the spectral bimodal distribution responses of the Unaffected, Wind-generated Waves, and Cloud Shading conditions in the region. In agreement with the boxplot analysis, across the five multispectral bands, the reflectance data reveal that the introduction of wind-generated waves and cloud shading conditions results in increased means and standard deviations, reductions in the prominence of both peaks and a broadening of the density curve's base, indicating a change in magnitude and variability of the affected reflectance data.

The CoV and SNR metrics provide additional insights: under cloud shading, there is a notable increase in CoV for most bands, accompanied by a decrease in SNR, except in the blue band. Conversely, under the influence of wind-generated waves, CoV decreases while SNR increases, reflecting a contrasting and unexpected pattern. Although these variations in CoV and SNR are relatively small and lack a strong trend, as observed in sun glint analysis, they underscore the subtle yet significant impact of these environmental factors on the UAS reflectance readings over the water surface.

The presence of two distinct peaks in the distribution is likely explained by the heterogeneous turbidity concentrations (from 17.8 to 79.1 FNU) within the upstream area or due to different solar elevation angles, since the images located in this area were acquired from 09:14 to 09:48, with solar elevation ranging from 45° to 55°. The latter is less probable because the three categories (Unaffected, Wind-generated Waves, and Cloud Shading) have samples well distributed along this time interval.

Furthermore, the observed spectral behavior in all upstream groups shows higher reflectance values in the Green and Red Edge and lower in Blue and Red, which is associated with the spectral response of chlorophyll-a in eutrophic waters [38]. The strong signal observed in the Red Edge band may be attributed to elevated turbidity levels, as this band has been recognized by several researchers as an effective indicator for monitoring turbidity or suspended solids in optically shallow regions [42,43]. The predominant Green and Red Edge spectra response is similar to the results of [44] using a Micasense RedEdge-M sensor in Lake Batalon and Kis Balaton (Hungary), with varied trophic status and suspended matter concentration, similar to the Pampulha Reservoir.

It is important to note that the accuracy of the correction steps could have been influenced by the spectral configuration mismatch between the Calibration Reflectance Panel (CRP) and the sensor, as the CRP was designed by Micasense while the sensor employed in this particular analysis was manufactured by DJI. This spectral misalignment may have contributed to inconsistencies in the radiometric calibration process. Additionally, the calibration on a day with intermittent cloud cover, rather than consistently overcast or completely sunny conditions, might have further impacted the accuracy of the reflectance data, potentially introducing variability that could obscure the distinctiveness of the unaffected downstream group as a control.

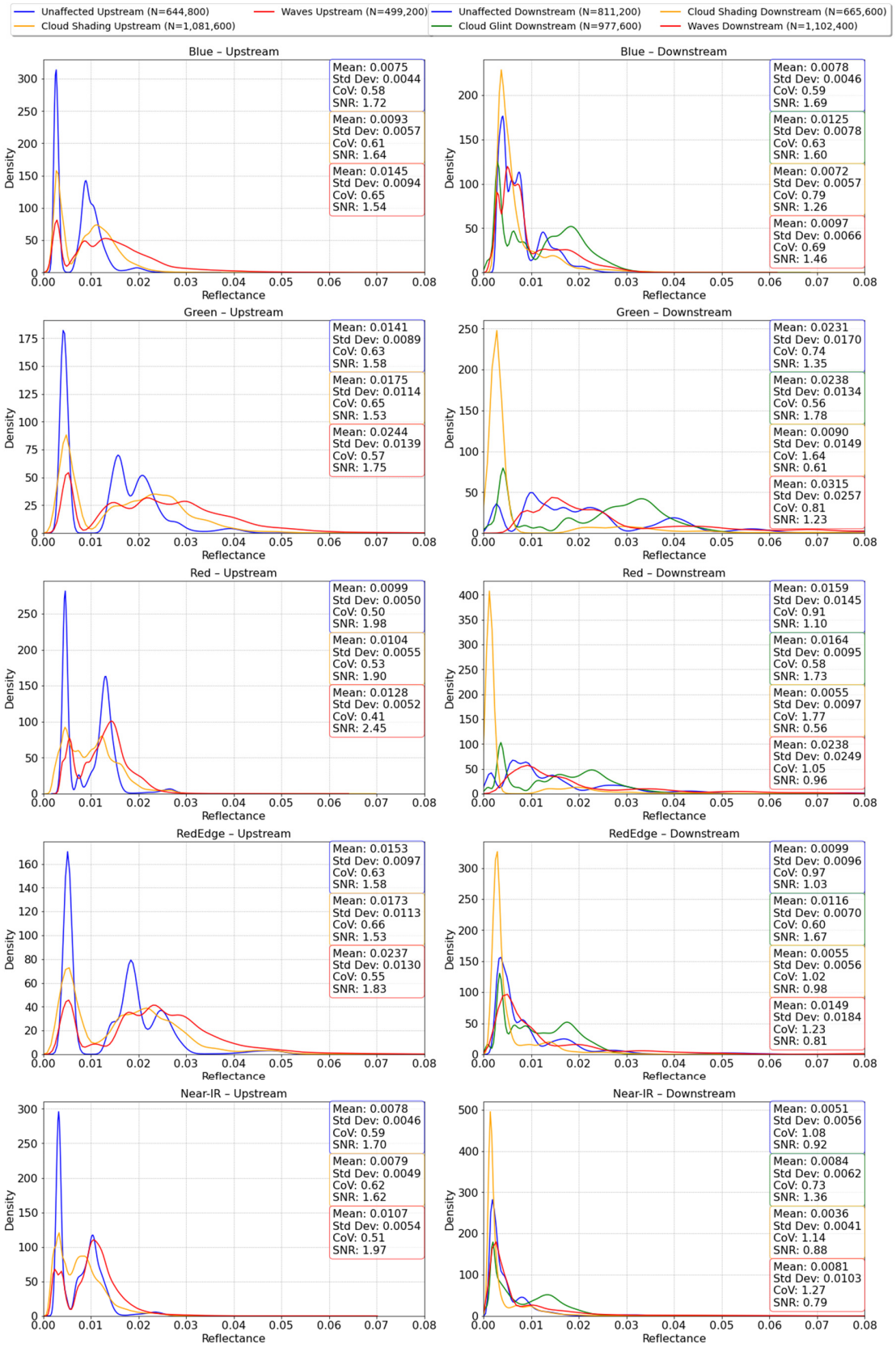

Figure 7. Probability density functions of reflectance from unaffected, cloud shading wind-generated waves and sky glint categories. Data were collected over the Pampulha Reservoir upstream (**left**) and downstream (**right**) of the net, on 10 March 2022.

3.2.2. Pampulha Reservoir—Downstream of the Net

Following the upstream analysis, which highlighted the significant influence of environmental conditions such as cloud shading and wave-induced variability on spectral reflectance, this section focuses on the downstream area of the Pampulha Reservoir. Besides those cited effects, cloud glints were perceived on images collected in the downstream area during the UAS survey on 10 March. Figure 7 (right) presents the PDFs and Figure 8 the boxplots illustrating the data distribution and statistical analysis in the study area.

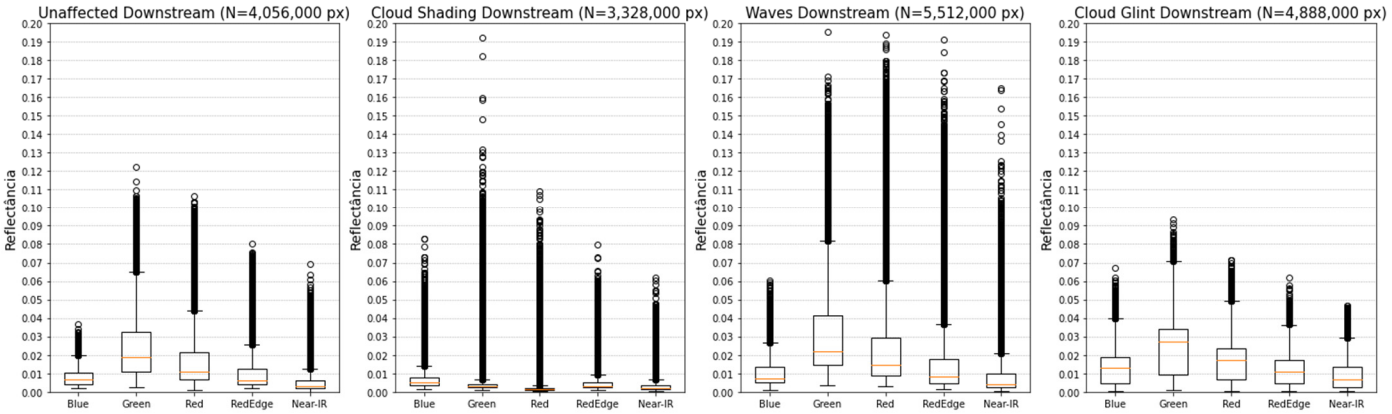

Figure 8. Boxplot analysis of pixel reflectance values under different environmental conditions at the Pampulha Reservoir (downstream) on 10 March 2022, collected with DJI P4M UAS. The orange line represents the median reflectance for each band, indicating the central tendency of the data distribution.

The unaffected downstream data were initially intended to serve as a control, with the expectation of consistent spectral patterns and lower variability compared to the affected groups. However, while the data did not reveal unique patterns in standard deviation, CoV, or SNR, it still provided a useful baseline for comparison. Images in this category were selected between 07:38 and 09:58 A.M. and were near water quality measurements (N = 6) that showed chlorophyll levels ranging from 7.4 to 9.1 RFU and turbidity between 5.1 and 13.3 NTU, suggesting a relatively stable environment. The Green band dominates the spectral response, likely due to the presence of chlorophyll algae in low-turbidity environments [37,38].

Regarding the downstream unaffected data, they showed lower reflectance in the Red Edge and Near-IR bands, along with higher reflectance in the Green band compared to the upstream unaffected data. This pattern is consistent with the characteristics of the Pampulha Reservoir, where chlorophyll predominantly influences the spectral behavior downstream of the net. Moreover, the greater disparity between the Green and Red bands in the downstream data accounts for the more distinct brownish hues in the upstream area and greenish hues in the downstream area.

The analysis of the downstream data under cloud shading conditions reveals a significant reduction in median reflectance values across all multispectral bands, accompanied by the most notable decrease in the interquartile range (IQR) compared to other conditions. This reduction in IQR results in higher density peaks in the distribution across the five bands (Figure 7 (right)). Additionally, even with this strong alteration in IQR the shaded downstream data boxplot exhibits higher and longer tails of upper outliers, which is a similar pattern observed in the upstream shaded data and in [20].

The spectral behavior observed under cloud shading deviates notably from the typical pattern seen in the downstream data, where green and red wavelengths generally exhibit the highest reflectance. This shift in spectral dominance could potentially be associated with variations in water quality; however, it is more likely caused by optical effects due to cloud shading. This is because the water quality conditions (N = 4), characterized by

relatively low levels of chlorophyll (7.4 to 10.6 RFU) and turbidity (5.0 to 7.0 NTU), are similar to those in unaffected downstream areas. Moreover, the solar elevation was also similar, with the cloud-shaded images and unaffected images well distributed between 08:35 and 10:06.

In contrast, the spectral responses downstream under the influence of wind-generated waves showed increased IQR, mean, and median reflectance values, as well as higher standard deviation and CoV, while SNR decreased. The boxplot also displays higher and longer upper outlier tails, indicating a broader distribution of reflectance values and increased variability. These findings are consistent with observations from wave-affected upstream Pampulha data and in [21].

The effects are likely due to the dynamic agitation of the water surface caused by the waves, as the images were taken between 07:35 and 08:39. Nearby water quality samples (N = 6) showed chlorophyll levels ranging from 8.7 to 10.6 RFU and turbidity between 6.2 and 9.6 NTU, similar to the unaffected downstream group. Despite the wave-induced agitation, the spectral behavior remains consistent with the unaffected downstream data, with the green band continuing to show the highest reflectance.

The downstream data influenced by cloud glint were the only ones to exhibit shorter upper outliers. However, the affected pixels showed an increase in maximum, mean, and median reflectance values. Despite this, no consistent pattern was observed in CoV, standard deviation, or SNR, highlighting the complex nature of spectral variability under cloud glint. Nonetheless, the dominant spectral behavior was maintained, with the green band continuing to exhibit the highest reflectance. Although the images were acquired between 07:34 and 09:28, water quality samples (N = 9) collected near these image coordinates showed chlorophyll concentrations ranging from 8.0 to 14.1 RFU and turbidity levels varying between 6.2 and 47.5 NTU, indicating that the images were captured under diverse water conditions. This was particularly evident for images near the sediment net, where turbidity was higher. Along with the effects of sky glint, these varying water quality conditions likely contributed to the increased central tendency and maximum values.

4. Discussions

4.1. Sun Glint

Among the degrading effects studied in this work, sun glint is the most discussed in the literature. The phenomenon is caused on the water's surface due to varying sun elevation angles and azimuth angles concerning the UAS sensor. It occurs when the sunlight incidence angle is equal to the reflection angle, causing specular reflections of direct sunlight onto the sensors [27,28,30,45]. To illustrate that the sun glint intensifies with the increase in the sun elevation angle, Figure 9 represents samples of imagery used in this study.

When observing that the minimum values on the 4th flight were lower than the ones from the earlier flights, it indicates that in the presence of intense sun glints, the sensor employs automatic exposure adjustment mechanisms to counter the effects of the overexposure condition, involving a reduction in the sensor's ISO sensitivity and narrowing the sensor aperture. Consequently, not only the area affected by the sun glint will reduce the reflectance values, but in the entire image, leading to pixels with lower signal readings in areas non affected by sun glints. This sensor behavior was also observed in cloud-shaded images in the Pampulha Reservoir.

Furthermore, as pointed out by [46], tilting the sensor up to 15° off-nadir allows it to diminish and move the sun glint to the edge of the images (Figure 10). However, changing the gimbal angle will also change the coordinates of the image's central point, which will no longer match the GPS point stored in the photo's metadata. For a flight at 40 m height, a 15° tilt in the gimbal will cause a displacement of approximately 10 m to the image coordinate system. In a flight at a height of 120 m, this displacement will be approximately 32 m. Depending on the size of the reservoir and the spatial scale of the RS application in development, it may be an issue.

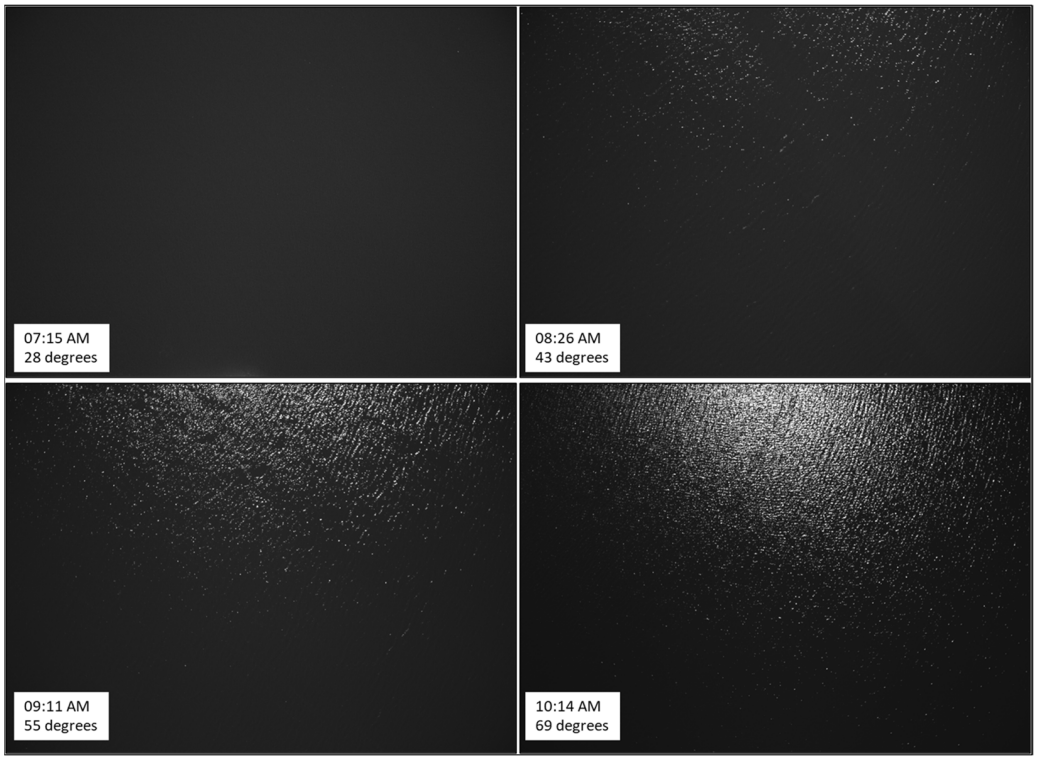

Figure 9. Near-Infrared images of the Vargem das Flores Reservoir, captured by the NUVEM-ALTUM UAS on 17 November 2021. Each image presents the collection time and sun elevation angle.

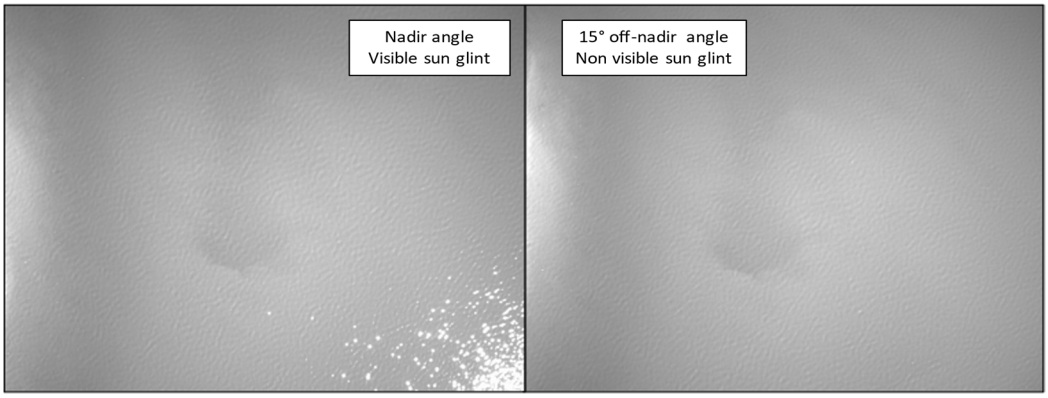

Figure 10. Reduction in sun glint effect when tilting the sensor up to 15 degrees off-nadir. Red-Edge images from DJI P4M UAS sensor, on the Pampulha Reservoir, on 14 September 2022, 09:44 AM. Sun's elevation angle was 51°. Images were taken at the same time, with a height of 40 m. The left image was taken with a nadir tilting angle (90°). The right image was taken with 75° (or 15° off-nadir).

For sun glint experimental tests in the present work, the alignment of the UAS sensor's azimuth angle with the average sun azimuth angle was successful in demonstrating the intensification of sun glint following the sun elevation angle. To avoid sun glint effects due to the sun's position, Ref. [27] recommended a minimum sun elevation angle of 30° and a maximum of 45°, while Ref. [29] recommended between 30° and 60°, and Ref. [28] suggested angles between 35° and up to 75°, when using glint removal procedures. Moreover, Ref. [30] recommended a maximum solar elevation of 90° minus ½ field of view (FOV) of the camera sensor, which in the case of the Micasense Altum (FOV = 62.7°) would be 58.7°.

Our findings suggest that the ideal time frame for capturing images over aquatic reservoirs with minimal sun glint can be broadened to a solar elevation angle ranging from 25° to 47°. Adhering to the recommended sun elevation angles is essential for reliable

UAS-based water reservoir reflectance measurements, thereby minimizing sun glint and improving data liability and accuracy.

4.2. Cloud Glints

When capturing UAS images of calm inland reservoirs, cloud glints can be reflected off the water surface into the sensor's field of view, resulting in glare from the clouds on the captured image. This phenomenon occurs due to the reflective properties of water, where the smooth surface acts like a mirror, reflecting the surrounding environment, including the sky, clouds, trees, and buildings. Under nearly full overcast conditions, the water surface reflects a uniform gray tone, while a few scattered clouds produce distinct, irregular reflections. Figure 11 illustrates this contrast.

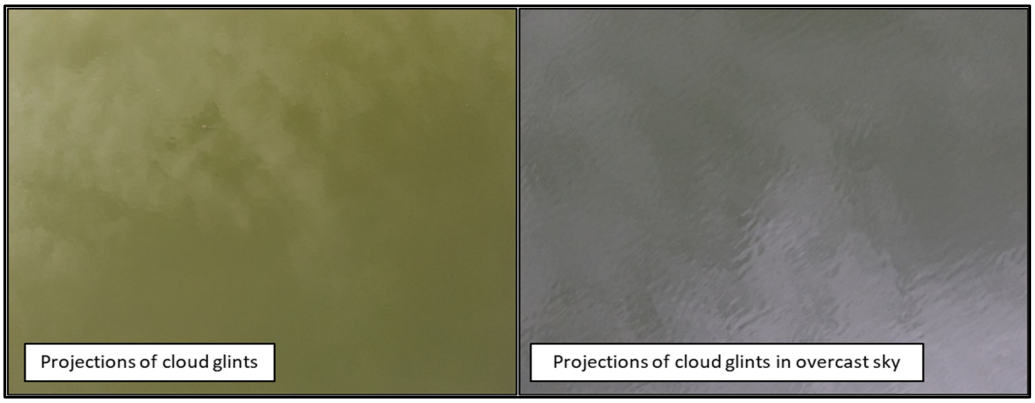

Figure 11. Samples of images with projections of clouds and gray sky reflex on the water surface. Images were collected with UAS DJI P4M RGB sensor, at the Pampulha Reservoir (downstream of the net), on 12 May 2022, between 10:14 and 10:19 AM, when the sun elevation angle was 45°.

The results of this study provide valuable insights into the complex interactions between cloud glint, spectral behavior, and water quality parameters in UAS imagery of inland reservoirs. The shorter upper outliers observed in the downstream data influenced by cloud glint suggest a potential attenuation effect on higher reflectance values. However, the increase in maximum, mean, and median reflectance values in affected pixels indicates that cloud glint can still amplify reflectance, likely due to enhanced light scattering.

The absence of a consistent pattern in the CoV, Std Dev, and SNR underscores the complexity of spectral variability under cloud glint conditions. This variability suggests that while cloud glint can alter the reflectance values, it does so in a non-uniform manner, complicating correction procedures.

A comprehensive comparison of the effects of sky glint on UAS images would benefit from data collected from areas with varying turbidity and pigment levels, including regions before the net sediment barrier in the Pampulha Reservoir. This study was limited to post-barrier areas, which constrained the scope of the findings.

4.3. Wind-Generated Waves

Waves cause glints by reflecting sunlight off the varying angles of the wave facets on the water's surface. As the surface of the water undulates due to wind-generated waves, these wave facets act like small mirrors that reflect sunlight. When the angle of a wave facet aligns with the direction of the incoming sunlight and the sensor's field of view, it results in bright spots, known as glint. This glint increases the apparent brightness in the captured images, leading to variability and noise in the reflectance data factors [16,47].

The findings of this study highlight the significant influence of wind-generated waves on the reflectance values captured by UAS in both upstream and downstream sections of the Pampulha Reservoir. Observed in both upstream and downstream areas, the increased variability and extremity in reflectance data caused by waves underscore these environmen-

tal factors' challenges to accurate remote sensing of aquatic environments. Moreover, the consistent pattern of elevated median and maximum reflectance values across all spectral bands suggests that the dynamic nature of waves introduces noise and variability into the data. However, due to consistency, algorithms that focus on addressing these changes have the potential to reduce interferences caused by waves.

Figure 12 illustrates the contrast in brightness between the crests and troughs of waves, caused by low-intensity sun glint resulting from variations in the angle of incidence. This visual evidence supports the observed changes in statistical metrics.

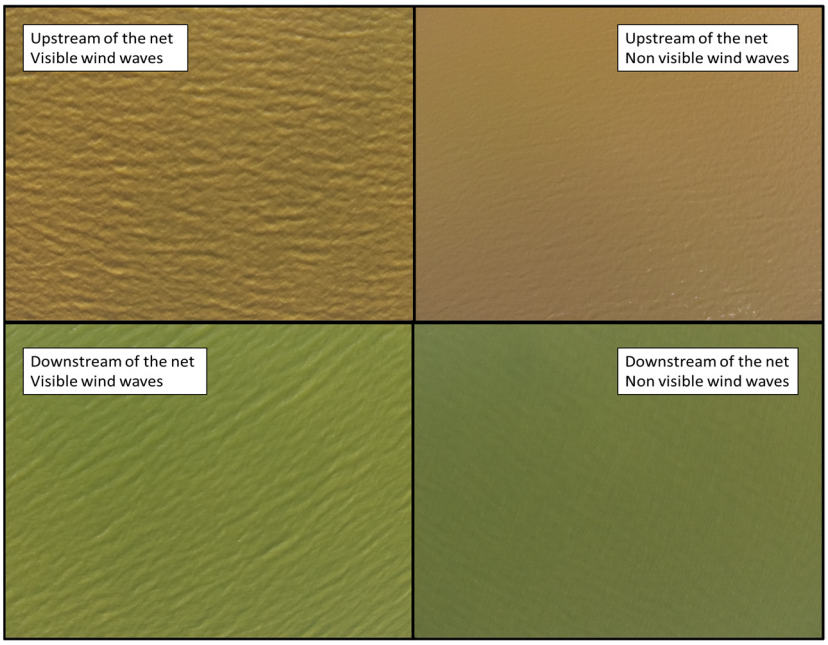

Figure 12. Aerial images show the contrast in brightness between the crest and trough of waves, caused by the low-intensity sun glint arising from variations in the angle of incidence. These samples were collected at the Pampulha Reservoir on 10 March 2022, by a DJI P4M UAS between 10:14 and 10:19 AM. The higher visibility of waves is due to differences in wind speed.

To mitigate the impact of waves on reflectance measurements, capturing images with the sensor positioned perpendicular to the wave propagation direction is recommended. This approach reduces the visibility of waves and their effects, as waves are more distinctly visible from the front or rear than from the side edges. Additionally, using a downward-looking (nadir) view minimizes the contrast between the crests and troughs of waves, further diminishing their impact on reflectance data [41].

The dynamic nature of wind-generated waves, shaped by variables like wind speed, wave height, water depth, and surface roughness, poses significant challenges for accurate UAS sensing. The complex interplay of these factors leads to unpredictable reflectance patterns, making it difficult to develop generalized algorithms for correction. Existing literature, such as studies on the classification of seaweed communities [48] and optical reflectance models for chlorophyll-a [49] and turbidity [50], highlights the complexities and obstacles posed by waves in remote sensing applications.

4.4. Cloud Shading Projections

The impact of cloud shading on UAS-based reflectance measurements reveals both subtle and complex interactions with the underlying water surface, particularly in areas with varying turbidity and chlorophyll concentrations. Effects observed upstream and downstream share few similarities, such as the reduction in minimum values and the shortening of the upper tail of outliers. However, there are clear distinctions, notably in the interquartile range (IQR) and changes in spectral behavior. No definitive patterns

were consistently observed, highlighting the unpredictable nature of cloud shading impacts. These findings agree with [28], who noted that abrupt illumination changes, such as those caused by entering a cloud-covered area, disrupt the homogeneity of spectral features, complicating the interpretation of derived spectral, structural, or classification-based data products.

Our results also align with those of [20], who described similar variability in reflectance data due to the unpredictable interactions between shadows and glint, which can either cancel each other out or cause sudden shifts in reflectance. This unpredictability, coupled with sensor sensitivity adjustments, explains both the reduced values in shaded regions and the presence of higher outliers in unaffected areas. These phenomena illustrate the nuanced challenges in interpreting UAS-based reflectance data. Moreover, our findings corroborate with [51], emphasizing that variable cloud cover can significantly affect the accuracy and signal-to-noise ratio (SNR) of reflectance measurements due to fluctuating illumination conditions. Under clear skies, reflectance is more stable and easier to model, but under cloudier conditions with diffuse illumination, reflectance measurements become increasingly difficult to interpret. Figure 13 illustrates how cloud shading projections impact the collected images.

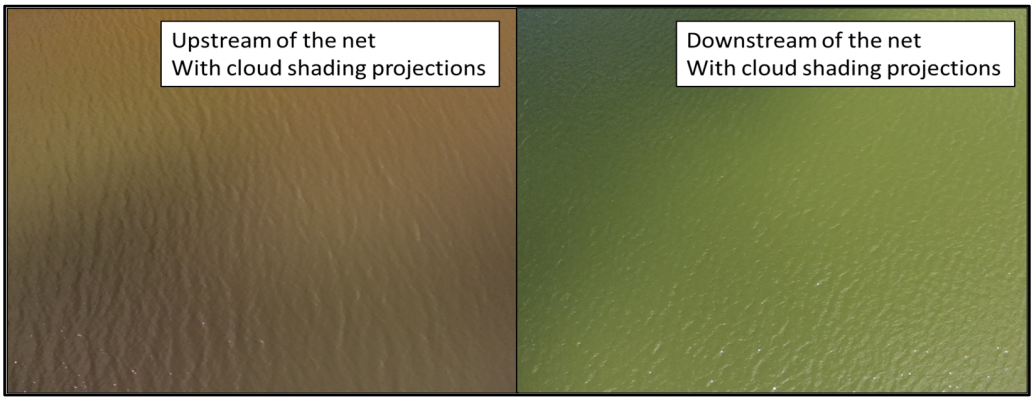

Figure 13. Aerial images show the dark areas caused by cloud shading projections. Images were collected at the Pampulha Reservoir, on 10 March 2022, by DJI P4M UAS, between 10:14 and 10:19 AM.

It is worth observing that the shadow cast by sudden clouds on the water surface jeopardizes the reflectance values because images will have misrepresented bright (no shading) and dark (shading) areas. In this case, the irradiance data collected by the DLS, which are used to calibrate the radiometry, do not represent the different irradiance on bright and dark areas, only at the image center (when the nadir tilting angle is 90°).

5. Conclusions

This study provides a comprehensive analysis of the impact of various environmental conditions on the reflectance values obtained from inland waters using multispectral UAS imagery. The findings highlight the significant influence of sun glints, cloud glints, wind-generated waves, and cloud shading on the accuracy and reliability of reflectance measurements.

The analysis of sun glint effects on UAS-based reflectance measurements revealed that as the sun's elevation angle increases, so does the intensity of sun glint, leading to significant variability in reflectance values across all spectral bands. The study found a systematic increase in the mean, standard deviation, and CoV of reflectance values with higher solar angles, particularly noticeable in the third and fourth flights where the solar elevation exceeded 54°. This variability introduces noise, reducing the SNR and potentially compromising data quality. The findings suggest that for accurate UAS-based water quality monitoring, flight operations should ideally occur within a solar elevation angle range of

25° to 47° to minimize sun glint effects. Proper geometry of sensor azimuth with the solar azimuth can further control these effects.

Cloud shading introduces complex and subtle changes in reflectance measurements, as observed in both upstream and downstream sections of the Pampulha Reservoir. The results indicate a general reduction in median reflectance values and increased variability in the presence of cloud shading. This effect is particularly challenging to correct due to the unpredictable nature of cloud movements and their impact on illumination conditions. The study found that cloud shading often leads to lower minimum reflectance values and shorter upper outliers, which can distort the overall spectral response. These findings emphasize the importance of considering cloud cover during UAS missions, as even slight changes in shading can significantly affect reflectance measurements and, consequently, the accuracy of water quality assessments.

Wind-generated waves were shown to introduce considerable variability in reflectance values by creating dynamic surface conditions that enhance sun glint and scatter light irregularly. The results demonstrated an increase in the mean, standard deviation, and CoV of reflectance values under wave-influenced conditions, with the spectral response showing higher reflectance values across all bands. This effect was consistently observed in both upstream and downstream sections of the Pampulha Reservoir.

The presence of cloud glints was found to amplify reflectance values by reflecting bright patches of cloud cover off the water surface into the UAS sensor's field of view. While this effect generally increases maximum and median reflectance values, it does so in a non-uniform manner, leading to unpredictable changes in data variability. The study observed that cloud glints resulted in higher maximum values but did not show a consistent trend in CoV or SNR, highlighting the complexity of correcting for this effect. The findings suggest that areas with varying turbidity and pigment levels may respond differently to cloud glints.

This research contributes valuable insights into the limitations and potential of using UAS for inland water monitoring. By identifying the specific environmental conditions that affect reflectance measurements, the study lays the groundwork for the development of more accurate correction methods and improved UAS deployment strategies. These advancements are crucial for enhancing the precision of environmental monitoring and supporting the sustainable management of water resources. Future studies should build on these findings by integrating them into broader monitoring frameworks and exploring the application of these insights in other types of aquatic environments.

Supplementary Materials: The following supporting information can be downloaded at: https://www.mdpi.com/article/10.3390/limnolrev24040027/s1, Figure S1. Boxplot analysis of pixels' reflectance values for five spectral bands (Blue, Green, Red, RedEdge, Near-IR) across four NUVAM-MICASENSE UAS flight times (07:02 AM, 08:21 AM, 09:09 AM, and 10:08 AM) on 17 November 2021, at Vargem das Flores Reservoir. The *Y*-axis in this figure is wider than Figure 4, particularly to illustrate the outliers between the first and second flights and between the third and fourth.

Author Contributions: D.H.C.S.: Conceptualization, Methodology, Software, Formal analysis, Investigation, Data Curation, Writing, Visualization. G.R.A.: Methodology, Software, Investigation. A.F.A.: Methodology, Software, Data Curation, Investigation. P.H.d.M.C.: Methodology, Software, Investigation. G.P.: Methodology, Writing (Review & Editing), Supervision. C.C.A.: Methodology, Writing (Review & Editing), Supervision, Project administration. All authors have read and agreed to the published version of the manuscript.

Funding: This research was funded by Companhia Energética de Minas Gerais (CEMIG), Project GT-0607, titled "Intelligent Water Quality Monitoring through the Development of Photo-optical Algorithm", and the National Council for Scientific and Technological Development (CNPQ) grant number 306373/2023-8.

Data Availability Statement: The data presented in this study are available on request.

Acknowledgments: The authors would like to express their sincere appreciation to CEMIG, CAPES (Coordination of Superior Level Staff Improvement), CNPQ and UFMG (Universidade Federal de Minas Gerais) for supporting the development of this research.

Conflicts of Interest: The authors state that they have no known financial conflicts of interest or personal relationships that could have influenced the work presented in this paper.

References

1. Pokrzywinski, K.; Johansen, R.; Reif, M.; Bourne, S.; Hammond, S.; Fernando, B. Remote sensing of the cyanobacteria life cycle: A mesocosm temporal assessment of a *Microcystis* sp. bloom using coincident unmanned aircraft system (UAS) hyperspectral imagery and ground sampling efforts. *Harmful Algae* **2022**, *117*, 102268. [CrossRef] [PubMed]
2. Chen, B.; Mu, X.; Chen, P.; Wang, B.; Choi, J.; Park, H.; Xu, S.; Wu, Y.; Yang, H. Machine learning-based inversion of water quality parameters in typical reach of the urban river by UAV multispectral data. *Ecol. Indic.* **2021**, *133*, 108434. [CrossRef]
3. Arias-Rodriguez, L.F.; Tüzün, U.F.; Duan, Z.; Huang, J.; Tuo, Y.; Disse, M. Global Water Quality of Inland Waters with Harmonized Landsat-8 and Sentinel-2 Using Cloud-Computed Machine Learning. *Remote Sens.* **2023**, *15*, 1390. [CrossRef]
4. Souza, A.P.; Oliveira, B.A.; Andrade, M.L.; Starling, M.C.V.; Pereira, A.H.; Maillard, P.; Nogueira, K.; dos Santos, J.A.; Amorim, C.C. Integrating remote sensing and machine learning to detect turbidity anomalies in hydroelectric reservoirs. *Sci. Total Environ.* **2023**, *902*, 165964. [CrossRef] [PubMed]
5. Cao, Z.; Ma, R.; Duan, H.; Pahlevan, N.; Melack, J.; Shen, M.; Xue, K. A machine learning approach to estimate chlorophyll-a from Landsat-8 measurements in inland lakes. *Remote Sens. Environ.* **2020**, *248*, 111974. [CrossRef]
6. Hossain, A.K.M.A.; Mathias, C.; Blanton, R. Remote sensing of turbidity in the tennessee river using landsat 8 satellite. *Remote Sens.* **2021**, *13*, 3785. [CrossRef]
7. Olmanson, L.G.; Page, B.P.; Finlay, J.; Brezonik, P.L.; Bauer, M.E.; Griffin, C.; Hozalski, R.M. Regional measurements and spatial/temporal analysis of CDOM in 10,000+ optically variable Minnesota lakes using Landsat 8 imagery. *Sci. Total Environ.* **2020**, *724*, 138141. [CrossRef]
8. Dev, P.J.; Sukenik, A.; Mishra, D.R.; Ostrovsky, I. Cyanobacterial pigment concentrations in inland waters: Novel semi-analytical algorithms for multi- and hyperspectral remote sensing data. *Sci. Total Environ.* **2022**, *805*, 150423. [CrossRef]
9. Greene, S.B.D.; LeFevre, G.H.; Markfort, C.D. Improving the spatial and temporal monitoring of cyanotoxins in Iowa lakes using a multiscale and multi-modal monitoring approach. *Sci. Total Environ.* **2021**, *760*, 143327. [CrossRef]
10. Maciel, D.A.; Barbosa, C.C.F.; Novo, E.M.L.d.M.; Júnior, R.F.; Begliomini, F.N. Water clarity in Brazilian water assessed using Sentinel-2 and machine learning methods. *ISPRS J. Photogramm. Remote Sens.* **2021**, *182*, 134–152. [CrossRef]
11. Yang, H.; Kong, J.; Hu, H.; Du, Y.; Gao, M.; Chen, F. A Review of Remote Sensing for Water Quality Retrieval: Progress and Challenges. *Remote Sens.* **2022**, *14*, 1770. [CrossRef]
12. Tian, D.; Zhao, X.; Gao, L.; Liang, Z.; Yang, Z.; Zhang, P.; Wu, Q.; Ren, K.; Li, R.; Yang, C.; et al. Estimation of water quality variables based on machine learning model and cluster analysis-based empirical model using multi-source remote sensing data in inland reservoirs, South China. *Environ. Pollut.* **2024**, *342*, 123104. [CrossRef] [PubMed]
13. Chen, P.; Wang, B.; Wu, Y.; Wang, Q.; Huang, Z.; Wang, C. Urban river water quality monitoring based on self-optimizing machine learning method using multi-source remote sensing data. *Ecol. Indic.* **2023**, *146*, 109750. [CrossRef]
14. Becker, R.H.; Sayers, M.; Dehm, D.; Shuchman, R.; Quintero, K.; Bosse, K.; Sawtell, R. Unmanned aerial system based spectroradiometer for monitoring harmful algal blooms: A new paradigm in water quality monitoring. *J. Great Lakes Res.* **2019**, *45*, 444–453. [CrossRef]
15. Wei, L.; Zhang, Y.; Huang, C.; Wang, Z.; Huang, Q.; Yin, F.; Guo, Y.; Cao, L. Inland Lakes Mapping for Monitoring Water Quality Using a Detail/Smoothing-Balanced Conditional. *Sensors* **2020**, *20*, 1345. [CrossRef]
16. Windle, A.E.; Silsbe, G.M. Evaluation of Unoccupied Aircraft System (UAS) Remote Sensing Reflectance Retrievals for Water Quality Monitoring in Coastal Waters. *Front. Environ. Sci.* **2021**, *9*, 674247. [CrossRef]
17. Vanhellemont, Q. Automated water surface temperature retrieval from Landsat 8/TIRS. *Remote Sens. Environ.* **2020**, *237*, 111518. [CrossRef]
18. Wang, S.; Li, J.; Zhang, B.; Lee, Z.; Spyrakos, E.; Feng, L.; Liu, C.; Zhao, H.; Wu, Y.; Zhu, L.; et al. Changes of water clarity in large lakes and reservoirs across China observed from long-term MODIS. *Remote Sens. Environ.* **2020**, *247*, 111949. [CrossRef]
19. Cheng, K.; Chan, S.; Lee, J.H. Remote sensing of coastal algal blooms using unmanned aerial vehicles (UAVs). *Mar. Pollut. Bull.* **2020**, *152*, 110889. [CrossRef]
20. Zeng, C.; Richardson, M.; King, D.J. The impacts of environmental variables on water reflectance measured using a lightweight unmanned aerial vehicle (UAV)-based spectrometer system. *ISPRS J. Photogramm. Remote Sens.* **2017**, *130*, 217–230. [CrossRef]
21. Tiškus, E.; Bučas, M.; Vaičiūtė, D.; Gintauskas, J.; Babrauskienė, I. An Evaluation of Sun-Glint Correction Methods for UAV-Derived Secchi Depth Estimations in Inland Water Bodies. *Drones* **2023**, *7*, 546. [CrossRef]
22. Xiao, Y.; Chen, J.; Xu, Y.; Guo, S.; Nie, X.; Guo, Y.; Li, X.; Hao, F.; Fu, Y.H. Monitoring of chlorophyll-a and suspended sediment concentrations in optically complex inland rivers using multisource remote sensing measurements. *Ecol. Indic.* **2023**, *155*, 111041. [CrossRef]

23. Qin, J.; Li, M.; Zhao, J.; Li, D.; Zhang, H.; Zhong, J. Advancing sun glint correction in high-resolution marine UAV RGB imagery for coral reef monitoring. *ISPRS J. Photogramm. Remote Sens.* **2024**, *207*, 298–311. [CrossRef]
24. Giles, A.B.; Davies, J.E.; Ren, K.; Kelaher, B. A deep learning algorithm to detect and classify sun glint from high-resolution aerial imagery over shallow marine environments. *ISPRS J. Photogramm. Remote Sens.* **2021**, *181*, 20–26. [CrossRef]
25. Lee, J.-S.; Baek, J.-Y.; Shin, J.; Kim, J.-S.; Jo, Y.-H. Suspended Sediment Concentration Estimation along Turbid Water Outflow Using a Multispectral Camera on an Unmanned Aerial Vehicle. *Remote Sens.* **2023**, *15*, 5540. [CrossRef]
26. Greco, M.K.B.; de Freitas, J.R. On two methods to estimate production of Eichhornia crassipes in the eutrophic Pampulha reservoir (MG, Brazil). *Braz. J. Biol.* **2002**, *62*, 463–471. [CrossRef]
27. Doukari, M.; Batsaris, M.; Papakonstantinou, A.; Topouzelis, K. A protocol for aerial survey in coastal areas using UAS. *Remote Sens.* **2019**, *11*, 1913. [CrossRef]
28. Trinh, H.L.; Kieu, H.T.; Pak, H.Y.; Pang, D.S.C.; Cokro, A.A.; Law, A.W.-K. A Framework for Survey Planning Using Portable Unmanned Aerial Vehicles (pUAVs) in Coastal Hydro-Environment. *Remote Sens.* **2022**, *14*, 2283. [CrossRef]
29. Cillero Castro, C.; Domínguez Gómez, J.A.; Delgado Martín, J.; Hinojo Sánchez, B.A.; Cereijo Arango, J.L.; Cheda Tuya, F.A.; Díaz-Varela, R. An UAV and Satellite Multispectral Data Approach to Monitor Water Quality in Small Reservoirs. *Remote Sens.* **2020**, *12*, 1514. [CrossRef]
30. Ortega-Terol, D.; Hernandez-Lopez, D.; Ballesteros, R.; Gonzalez-Aguilera, D. Automatic hotspot and sun glint detection in UAV multispectral images. *Sensors* **2017**, *17*, 2352. [CrossRef]
31. Komárek, J.; Klápště, P.; Hrach, K.; Klouček, T. The Potential of Widespread UAV Cameras in the Identification of Conifers and the Delineation of Their Crowns. *Forests* **2022**, *13*, 710. [CrossRef]
32. Di Gennaro, S.F.; Toscano, P.; Gatti, M.; Poni, S.; Berton, A.; Matese, A. Spectral Comparison of UAV-Based Hyper and Multispectral Cameras for Precision Viticulture. *Remote Sens.* **2022**, *14*, 449. [CrossRef]
33. McEliece, R.; Hinz, S.; Guarini, J.-M.; Coston-Guarini, J. Evaluation of nearshore and offshore water quality assessment using UAV multispectral imagery. *Remote Sens.* **2020**, *12*, 2258. [CrossRef]
34. Moshtaghi, M.; Knaeps, E.; Sterckx, S.; Garaba, S.; Meire, D. Spectral reflectance of marine macroplastics in the VNIR and SWIR measured in a controlled environment. *Sci. Rep.* **2021**, *11*, 5436. [CrossRef] [PubMed]
35. Shafiee, S.; Mroz, T.; Burud, I.; Lillemo, M. Evaluation of UAV multispectral cameras for yield and biomass prediction in wheat under different sun elevation angles and phenological stages. *Comput. Electron. Agric.* **2023**, *210*, 107874. [CrossRef]
36. Wang, C. At-sensor radiometric correction of a multispectral camera (Rededge) for suas vegetation mapping. *Sensors* **2021**, *21*, 8224. [CrossRef]
37. Chen, J.; Chen, S.; Fu, R.; Wang, C.; Li, D.; Peng, Y.; Wang, L.; Jiang, H.; Zheng, Q. Remote Sensing Estimation of Chlorophyll-A in Case-II Waters of Coastal Areas: Three-Band Model Versus Genetic Algorithm-Artificial Neural Networks Model. *IEEE J. Sel. Top. Appl. Earth Obs. Remote Sens.* **2021**, *14*, 3640–3658. [CrossRef]
38. Lu, L.; Gong, Z.; Liang, Y.; Liang, S. Retrieval of Chlorophyll-a Concentrations of Class II Water Bodies of Inland Lakes and Reservoirs Based on ZY1-02D Satellite Hyperspectral Data. *Remote Sens.* **2022**, *14*, 1842. [CrossRef]
39. Gao, B.-C.; Li, R.-R. Correction of Sunglint Effects in High Spatial Resolution Hyperspectral Imagery Using SWIR or NIR Bands and Taking Account of Spectral Variation of Refractive Index of Water. *Adv. Environ. Eng. Res.* **2021**, *2*, 1–15. [CrossRef]
40. Bielski, A.; Toś, C. Remote Sensing of the Water Quality Parameters for a Shallow Dam Reservoir. *Appl. Sci.* **2022**, *12*, 6734. [CrossRef]
41. Almar, R.; Blenkinsopp, C.; Almeida, L.P.; Catalán, P.A.; Bergsma, E.; Cienfuegos, R.; Viet, N.T. A new remote predictor of wave reflection based on runup asymmetry. *Estuar. Coast. Shelf Sci.* **2019**, *217*, 1–8. [CrossRef]
42. Pahlevan, N.; Sarkar, S.; Franz, B.; Balasubramanian, S.; He, J. Sentinel-2 MultiSpectral Instrument (MSI) data processing for aquatic science applications: Demonstrations and validations. *Remote Sens. Environ.* **2017**, *201*, 47–56. [CrossRef]
43. Caballero, I.; Stumpf, R.P. Towards routine mapping of shallow bathymetry in environments with variable turbidity: Contribution of sentinel-2A/B satellites mission. *Remote Sens.* **2020**, *12*, 451. [CrossRef]
44. De Keukelaere, L.; Moelans, R.; Knaeps, E.; Sterckx, S.; Reusen, I.; De Munck, D.; Simis, S.G.; Constantinescu, A.M.; Scrieciu, A.; Katsouras, G.; et al. Airborne Drones for Water Quality Mapping in Inland, Transitional and Coastal Waters—MapEO Water Data Processing and Validation. *Remote Sens.* **2023**, *15*, 1345. [CrossRef]
45. Muslim, A.M.; Chong, W.S.; Safuan, C.D.M.; Khalil, I.; Hossain, M.S. Coral reef mapping of UAV: A comparison of sun glint correction methods. *Remote Sens.* **2019**, *11*, 2422. [CrossRef]
46. Joyce, K.E.; Duce, S.; Leahy, S.M.; Leon, J.; Maier, S.W. Principles and practice of acquiring drone-based image data in marine environments. *Mar. Freshw. Res.* **2019**, *70*, 952–963. [CrossRef]
47. Mobley, C.D. Polarized reflectance and transmittance properties of windblown sea surfaces. *Appl. Opt.* **2015**, *54*, 4828. [CrossRef]
48. Cavanaugh, K.C.; Bell, T.W.; Hockridge, E.G. An Automated Method for Mapping Giant Kelp Canopy Dynamics from UAV. *Front. Environ. Sci.* **2021**, *8*, 587354. [CrossRef]
49. Gai, Y.; Yu, D.; Zhou, Y.; Yang, L.; Chen, C.; Chen, J. An improved model for chlorophyll-a concentration retrieval in coastal waters based on uav-borne hyperspectral imagery: A case study in qingdao, china. *Water* **2020**, *12*, 2769. [CrossRef]

50. Cai, J.; Meng, L.; Liu, H.; Chen, J.; Xing, Q. Estimating Chemical Oxygen Demand in estuarine urban rivers using unmanned aerial vehicle hyperspectral images. *Ecol. Indic.* **2022**, *139*, 108936. [CrossRef]
51. Arroyo-Mora, J.P.; Kalacska, M.; Løke, T.; Schläpfer, D.; Coops, N.C.; Lucanus, O.; Leblanc, G. Assessing the impact of illumination on UAV pushbroom hyperspectral imagery collected under various cloud cover conditions. *Remote Sens. Environ.* **2021**, *258*, 112396. [CrossRef]